Journal of Materials Processing Tech. 278 (2020) 116469

Contents lists available at ScienceDirect

Journal of Materials Processing Tech.

journal homepage: www.elsevier.com/locate/jmatprotec

Multiphysics modeling of continuous casting of stainless steel

Matthew L.S. Zappulla[a,b], Seong-Mook Cho[a], Seid Koric[b,c], Hyoung-Jun Lee[d], Seon-Hyo Kim[d], Brian G. Thomas[a,b,*]

[a] Mechanical Engineering, Colorado School of Mines, 1610 Illinois St., Golden, CO, 80401, USA
[b] Mechanical Science and Engineering, University of Illinois at Urbana-Champaign, 1260 W. Green St., Urbana, IL, 61801, USA
[c] National Center for Supercomputing Applications, University of Illinois at Urbana-Champaign, Urbana, IL, 61801, USA
[d] Materials Science and Engineering, Pohang University of Science and Technology, Pohang, Gyeongbuk, 37673, Republic of Korea

ARTICLE INFO

Associate Editor: A Luo

Keywords:
Constitutive models
Elastic-viscoplastic material
Finite element method
Solidification
Steel casting
Thermal stress

ABSTRACT

During the solidification of stainless steel, the mechanical behavior of the solidifying shell follows nonlinear elastic-viscoplastic constitutive laws depending on metallurgical phase fraction calculations (liquid, ferrite and austenite). A multiphysics model that couples thermal and mechanical behavior in a Lagrangian reference frame, including both classical time-independent plasticity and creep, with turbulent fluid flow in the liquid phase in an Eulerian frame, is applied to determine realistic temperature and stress distributions in the solidifying shell of stainless steel in a commercial continuous caster. Compositional effects are incorporated through the use of phase diagrams to define the phase fraction variations with temperature during the process. The behavior at these high temperatures can be adequately captured using specific constitutive equations for each phase and careful decisions about switching between them. Results for a 409L ferritic stainless steel show that, due to its phase fraction history, solidification stresses differ significantly from those in plain carbon steels. Specifically, they include a secondary sub-surface compression peak due to phase change expansion between γ-austenite and δ-ferrite through the thickness of the shell.

1. Introduction

While developments in advanced manufacturing processes, such as metal-based additive manufacturing are ongoing, the manufacturing field is still dominated by more traditional metal solidification processes, such as: ingot and foundry casting, welding, and particularly continuous casting. Advancement of these mature processes depends on improved quantitative understanding, such as that gained from advanced computational models. These processes are driven by many coupled phenomena, including heat transfer, fluid flow with turbulence, phase transformations, thermal distortion, and thermo-mechanical stress development.

Over 96 % of the world's steel is made with the continuous casting process, according to recent statistics by (World Steel Association, 2017). Experiments are limited due to the harsh conditions inside the liquid and solidifying steel, and the many process variables which affect the complex phenomena in the process. Thus, numerical modeling presents an ideal tool to better understand and help to find ways to reduce defects, increase productivity, and improve this important process. Tremendous advances in high performance computing technology and numerical algorithms in the last 25 years have enabled more realistic and accurate modeling of liquid steel flow and the solidifying shell, but finding multiphysics computational approaches that are both efficient and accurate remains a big challenge. Chronic defects affecting this process include cracking and surface depression problems, which often correspond to mismatches between solidification contraction and mold taper. (Zappulla and Thomas, 2017) have shown how this can increase the size of the solid shell/mold interfacial gap, which reduces heat transfer between the mold plate and steel shell, leading to locally hot and thin portions of the shell. These thin spots cause stress concentration, resulting in depressions, longitudinal cracks, and sometimes even breakouts, due to ferrostatic pressure from the liquid pool exerted onto the thin and weakened shell at mold exit.

Elastic, rate-independent plastic constitutive models are generally adequate for engineering purposes at ambient temperatures for most metallic materials. However, at high temperatures, most metal alloys exhibit time-dependent inelastic behavior, similar to a viscous fluid, and solidification adds further complication. Therefore, better constitutive models are needed to describe the elastic-viscoplastic behavior during metal solidification processes such as the continuous casting of steel.

* Corresponding author at: Mechanical Engineering, Colorado School of Mines, 1610 Illinois St., Golden, CO, 80401, USA
E-mail address: bgthomas@mines.edu (B.G. Thomas).

https://doi.org/10.1016/j.jmatprotec.2019.116469
Received 10 May 2019; Received in revised form 4 September 2019; Accepted 21 October 2019
Available online 26 November 2019
0924-0136/

1.1. Constitutive modeling of metal solidification

An important analytical solution for the generation of thermal stresses in a general one-dimensional metal solidification process was derived by (Weiner and Boley, 1963) using a simple elastic rate-independent plastic constitutive model. (Kristiansson, 1982) later added a creep law to account for the time-dependent inelastic behavior at high temperatures. In the last two decades, more fundamental but computationally demanding viscoplastic models, with and without yield surfaces, have been used to model realistic vertical-type semi-continuous aluminum direct-chill (DC) casting and steel continuous-casting processes. (Inoue and Ju, 1992) used a modification of Perzyna's constitutive equation to model elastic-viscoplastic constitutive behavior during aluminum DC casting. (Celentano, 2002) derived a yield-surface-based viscoplastic model with microstructure evolution and applied it to aluminum casting. (Paquet et al., 2011) incorporated rate-dependent behavior by using a viscoplastic model based on overstress in their homogenization model of cast aluminum alloys.

Unified viscoplastic constitutive models, which treat rate-independent plastic strain and rate-dependent creep together as inelastic strain, are particularly popular in steel casting. (Anand, 1982) developed the first such model based on several evolving internal state variables, that has been used in several thermo-mechanical models of metals on elevated temperatures. A decade later, (Kozlowski et al., 1992) introduced a simple constitutive equation to model the austenite phase of steel, relating inelastic strain, as a single structure parameter, to strain rate, stress, temperature, and steel grade via carbon content. To model the weaker, body-centered cubic (BCC) δ-ferrite phase of steel, (Zhu, 1996) devised a power law based constitutive model to incorporate the much higher creep rates of this phase, compared to the stronger, face-centered cubic (FCC) austenite phase. These constitutive models have been popular since their inception, having been either used or reviewed in many steel solidification papers, such as by (Huespe et al., 2000), (Li and Thomas, 2004), (Koric and Thomas 2006), (Groza et al., 2007), (Safari et al., 2013), (Qin et al., 2018). (Huespe et al., 2000) and later (Koric and Thomas, 2008) compared the Anand and Kozlowski-Zhu models against steel solidification experiments and found similar behavior for both models; although the Kozlowski-Zhu model produced results much closer to experiments for low carbon steels. (Pierer et al., 2005) also found that the Kozlowski model agreed well with several other steel solidification constitutive models and experiments.

In order to efficiently incorporate these highly nonlinear constitutive models at the local level (integration points), (Koric and Thomas, 2006) incorporated a bounded Newton-Raphson method at the integration points, into the global-level finite-element solution methodology in ABAQUS, which provided a tenfold performance increase in solving solidification thermo-mechanical problems. This approach is used in the current work. (Koric et al., 2009) later developed an explicit finite-element formulation of this method, and showed its benefits over the implicit method for large three-dimensional solidification problems with regard to high performance computing.

1.2. Multiphysics approaches

Turbulent fluid flow of molten steel with heat advection and thermo-mechanical behavior of the solidifying shell are traditionally modeled independently, with separate numerical methods (finite volume vs. finite element) and reference frames (Eulerian vs. Lagrangian). (Lee et al., 2000) followed by (Teskeredžić et al., 2002) have applied full coupling of these phenomena in a multiphysics frame on simplified casting geometries, but did not compare results with either analytical solutions or experiments. Another multiphysics approach to couple these phenomena is to focus on the solidification front to separate the fluid flow and thermo-mechanical models. The temporal and spatial distribution of superheat flux calculated to exit the solidification-front walls of the domain used by the thermal turbulent flow simulation can be implemented into the thermo-mechanical model of the solidifying steel shell growing in the mold region with a domain that includes only a portion of the fluid region. Because the mechanical behavior has minimal influence on the fluid flow, the two models are only one-way coupled, which enables significant computational savings.

(Koric et al., 2010b) devised and validated a new enhanced latent heat method to introduce spatial and temporal superheat flux data into a Lagrangian thermo-mechanical finite-element model of the solidifying shell and mold. The new modeling approach was demonstrated by (Koric et al., 2010a) via simulation of the multiphysics phenomena in a commercial continuous beam-blank casting of carbon steel grades, and the predictions show good matches with both an analytical solution to a one-dimensional test problem and with plant measurements of shell thickness profiles from a commercial caster.

For thermo-mechanical modeling of stainless steel alloys, most previous works have focused on various phenomena lower than solidification temperatures while only (Palumbo et al., 2015) and (Safari et al., 2013) have treated solidification of stainless steel grades but without any coupling with the fluid flow physics.

Regardless of the method, multiphysics modeling of solidification processes is a complex task. Phase-transformation laws are strongly dependent on chemical composition, and often differ between heating and cooling. Another issue is the lack of reliable thermo-mechanical properties in the literature for stainless steel at high temperature and low strain rate, which often leads to neglecting the phase dependence of the steel properties. We believe that this paper presents the first complete macro-scale model of stainless steel casting that couples thermo-mechanical analysis in solidifying stainless steel, based on thermo-elastic-viscoplastic phase dependent constitutive laws, with the turbulent thermal fluid flow of liquid steel, and thermal-mechanical deformation of the mold. This work presents a combined multiphysics modeling methodology for solidification processes, featuring a constitutive model where the compositional effects depend only on the phase fraction evolution, as well as a procedure to capture the important effects of heat transfer, turbulent fluid flow, and solidification on the thermo-mechanical behavior.

2. Multiphysics model formulation

The solidifying steel shell behavior is simulated here with a sophisticated, and computationally intensive, multiphysics model with several sub-models incorporating together a thermo-mechanical model of the solidifying steel shell (Section 2.1), a turbulent thermal fluid flow model of the liquid steel (Section 2.2), and a model of thermal distortion of the mold (Section 2.3), as shown in Fig. 1. In addition to their mechanical coupling, the shell and mold models are coupled thermally via a detailed model of the interfacial gap (Section 2.4). A validated heat transfer-solidification model CON1D, described by (Meng and Thomas, 2003), is used to provide the initial shell thickness profile for the fluid flow model and initial heat fluxes for the mold distortion model. The calculated heat fluxes due to the effect of superheat transport in the turbulent fluid flow model are incorporated into the thermo-mechanical model via the enhanced latent heat method, described in more detail in Section 2.2. In addition to this thermal coupling, the mechanical effect of fluid flow on the deformation of the solidified shell is considered by applying the ferrostatic pressure load that pushes the newly solidifying shell toward the mold, discussed in Section 2.4. Since the improved shell profile from thermo-mechanical model has little effect on superheat results in the fluid flow model, a single iteration of this model system is often sufficient to produce accurate multiphysics results.

2.1. Solidifying shell model

In many solidification processes, such as the continuous casting of

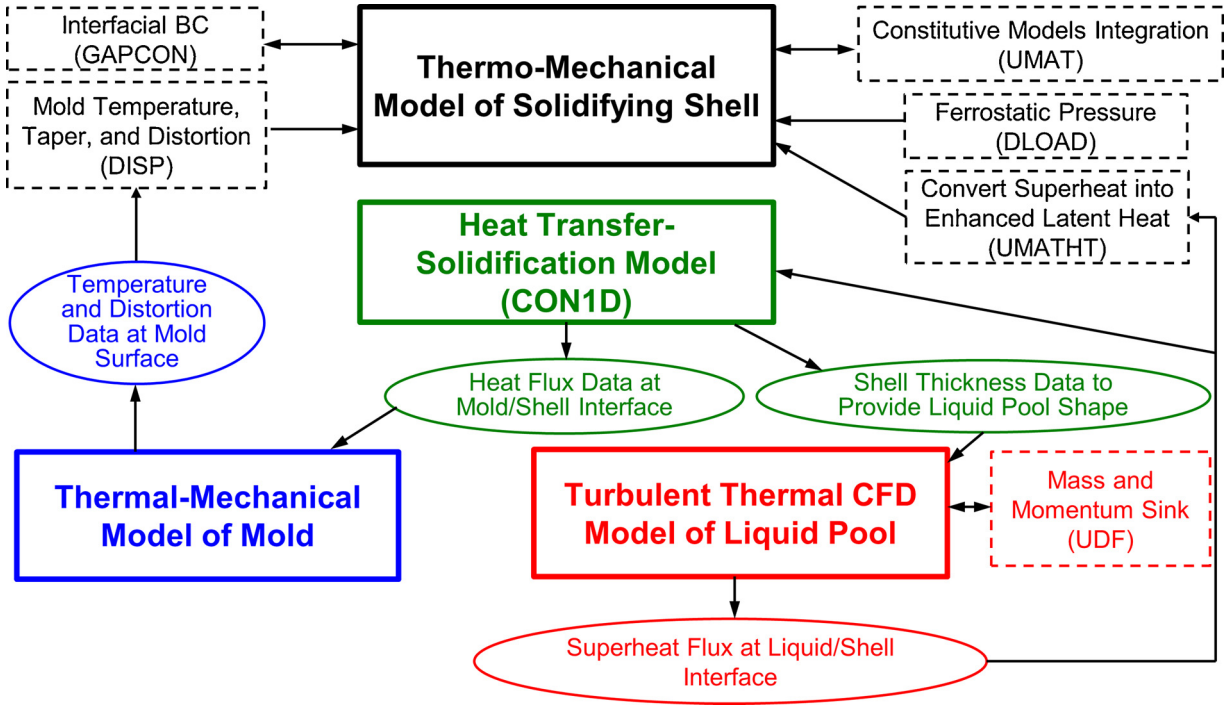

Fig. 1. Flow chart for multiphysics model.

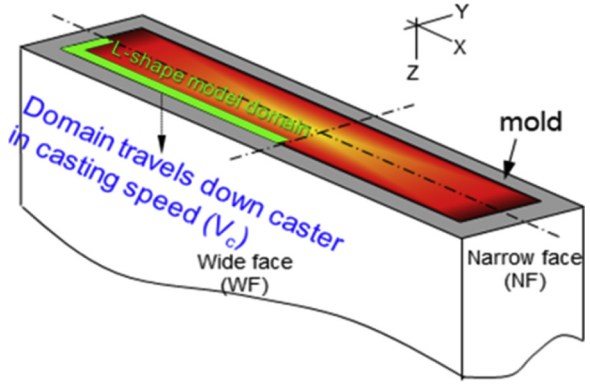

Fig. 2. Model domain of solidifying steel shell.

steel, one dimension of the casting is much longer than the others, and is otherwise unconstrained. In this case, it is quite reasonable to apply a condition of generalized plane strain (also called 2.5D model) in the long casting direction (z), and to solve a two-dimensional thermo-mechanical problem in the transverse (x-y) plane. (Koric et al., 2009) and others have demonstrated how this condition enables a two-dimensional computation to accurately produce the complete three-dimensional thermal-stress state, so long as there is no axial bending, as in the case here. A transverse Lagrangian generalized-plane-strain two-dimensional (2D) slice model, shown in Fig. 2, is applied to simulate the solidifying steel shell in the slab mold during continuous casting, which travels down the mold at the casting velocity. The domain is an L-shape of a ¼ strand section next to the mold wall which is thick enough to model double the expected thickness of the solidifying shell at mold exit. This approach avoids unnecessary and computationally intensive calculation of the liquid behavior away from the mold wall. More importantly, it avoids non-physical mass conservation by enabling shrinkage of the unmodeled liquid region due to pushing fluid out of the slice.

From the work of (Zappulla et al., 2017), a second "1D-slice" shell model was used to verify thermal stress behavior in simplified conditions. This slice model is seen as a thin strip "drilled" into the solidifying shell, and assumes uniform solidification and full contact with the mold wall.

In the Lagrangian reference frame, the temperature distribution in the strand is obtained from numerical solution of the three-dimensional (3D) transient heat conduction equation:

$$\rho\left(\frac{\partial H}{\partial t}\right) = \nabla\cdot(k\nabla T) \tag{1}$$

where ρ is the mass density, H is specific enthalpy, which includes the latent heat of phase transformations (solidification, and δ-ferrite to austenite), and k is the isotropic thermal conductivity. All of these properties are highly temperature dependent.

The strains during solidification are typically small (< 2 %), but the capability to handle finite rotations is necessary to model some parts of the shell in a continuous-casting process. The quasi-static equilibrium equation describes the mechanical behavior of the strand:

$$\nabla\cdot\boldsymbol{\sigma}(\boldsymbol{x}) + \boldsymbol{b} = \mathbf{0} \tag{2}$$

where $\boldsymbol{\sigma}$ is the Cauchy stress tensor and $\boldsymbol{b}$ is the body force density vector due to gravity. These equations were solved in a fixed finite-element mesh using the commercial stress software, ABAQUS (ABAQUS, 2013).

2.2. Fluid flow model and fluid/shell interface treatment

A 3D thermal turbulent fluid flow model of the molten steel pool is solved in an Eulerian reference frame for velocity and temperature fields, and superheat flux distributions at the steel shell front. The model domain includes the tundish bottom, nozzle, and top three-meters of the molten steel pool both in the strand and mold. The continuity equation that represents the mass conservation of the molten steel is given as follows:

$$\rho(\nabla\cdot\mathbf{v}) = S_m \tag{3}$$

where ρ is the mass density of liquid steel and $\mathbf{v}$ is time-average velocity, and S_m is a mass sink to model the liquid lost due to crossing the solidification front. This term is applied only to the computational cells

on the solidification front, according to the methodology of (Yuan et al., 2004).

Momentum conservation is satisfied by solving the time-averaged momentum balance:

$$\rho\left[\frac{\partial \mathbf{v}}{\partial t} + \mathbf{v}\cdot(\nabla \mathbf{v})\right] = \nabla\cdot\boldsymbol{\sigma} + \mathbf{S_{mom}} \tag{4}$$

where the Cauchy stress $\boldsymbol{\sigma}$ is represented by the standard constitutive relationship for turbulence:

$$\boldsymbol{\sigma} = C_{\mu}\frac{K^2}{\varepsilon}(\nabla \mathbf{v} + (\nabla \mathbf{v})^T) - p\mathbf{I} \tag{5}$$

where p is pressure, constant $C_{\mu}$is 0.09; K is turbulent kinetic energy, and ε is its dissipation rate, which are found by solving two additional partial differential equations according to the standard $K-\varepsilon$ model by (Launder and Spalding, 1974). $\mathbf{I}$ is the identity tensor. $\mathbf{S_{mom}}$ is a momentum sink term added to the same interface cells as S_m to account for solidification of the molten steel as explained by (Yuan et al., 2004).

Boundary conditions are fixed velocity at the inlet, no-slip conditions on the top surface beneath the slag layer, and on the walls which represent the solidification front, and pressure outlet conditions at the strand exit. The energy conservation equation for molten steel flow, which includes advection terms into Eq. (1), is:

$$\rho\left[\frac{\partial H}{\partial t} + \mathbf{v}\cdot\nabla H\right] = \nabla\cdot(k\nabla T) \tag{6}$$

Temperature was fixed to the liquidus temperature on the domain boundaries representing the solidification front that surrounds the liquid pool. These equations were solved using the commercial Computational Fluid Dynamics (CFD) software package, ANSYS Fluent (ANSYS et al., 2012)

According to the method of (Koric et al., 2010a), additional latent heat ΔH_f is calculated to represent superheat flux q''_{super}transported by the molten steel flow to the solidification front, based on the Stefan interface condition:

$$\Delta H_f = \frac{q''_{super}}{\rho_{solid}\ |\mathbf{v}_{interface}|} \tag{7}$$

This ΔH_f is additional latent heat added to the enthalpy in Eq. (1) via a user subroutine UMATHT in (ABAQUS, 2013). The discrete data of the superheat flux distribution, that is calculated at the boundaries of the 3-D Eulerian fluid flow model, is converted via multi-dimensional interpolation to a function of space and time (or distance below meniscus) for the mushy zone material points in the Lagrangian thermo-mechanical model as described by (Koric et al., 2010b). The solidification front velocity $\mathbf{v}_{interface}$ is calculated analytically according to (Koric et al., 2010a), based on the classic analytical solution for solid-control solidification with superheat from (Dantzig and Tucker, 2001).

2.3. Mold distortion model

As the solidifying steel shell moves down in the casting direction, heat leaving its surface is continuously extracted by water-cooling that flows through rectangular slots and channels in the copper mold. The mold also supports the steel shell and determines the shell shape. In this multiphysics model, a separate 3D finite-element model of a symmetric quarter of the mold system was developed to consider the influences of narrow face mold distortion and different mold surface temperatures. The mold geometry includes taper of the mold narrow face, which is applied to accommodate shrinkage of the solid steel shell. This methodology has been used in previous work by (Hibbeler et al., 2012). In addition to calculating the temperature, this model also calculates thermal distortion of the mold, which is applied with its taper as a boundary condition on the contact surface of the solidifying shell model via the DISP subroutine in ABAQUS. The shell solidification model in turn provides heat flux as a thermal boundary condition for this model, as presented in Fig. 1.

2.4. Boundary conditions and shell/mold interface treatment

Full thermal-mechanical coupling between the mold and solidifying steel shell is applied in this multiphysics model system to find the heat transferred across the interfacial gap, which in turn greatly depends on the gap size calculated from the mechanical solution. As the shell cools and shrinks, an air gap may open up near the corners due to non-optimized mold taper. Gap formation greatly affects final product quality, especially if it causes insufficient heat removal, a thinner shell, and defects such as longitudinal cracks, or even a catastrophic breakout if the molten steel penetrates through the shell. In this work, a resistor model is used to calculate heat transport across the interfacial gap. To find accurate interfacial heat fluxes, measurements of mold thermocouple temperatures and heat flux from water heatup are needed. For some previous models, such as (Şahin et al., 2006), (Cheung et al., 2009) and (Bertelli et al., 2016), an inverse heat conduction problem (IHCP) is solved to match the surface boundary conditions with specific plant measurements. In the current work, the two-way thermal-mechanical coupling between the solidifying steel shell and mold is modeled in detail to find the heat transferred across the interfacial gap between the mold and steel shell, which depends strongly on the local gap distance calculated from the mechanical solution. Measurements are used here for model calibration and validation.

The gap heat flux, q_{gap}, includes two parallel contributions, from radiation, h_{rad}, and conduction, h_{cond}:

$$q_{gap} = -k\partial T/\partial \boldsymbol{n} = -(h_{rad} + h_{cond})(T_{shell} - T_{mold}) \tag{8}$$

where $\boldsymbol{n}$ is the normal surface unit vector. The heat transfer coefficient due to radiation through the semi-transparent liquid part of the slag is:

$$h_{rad} = \frac{\sigma_{SB}}{\frac{1}{\varepsilon_{shell}} + \frac{1}{\varepsilon_{mold}} - 1}(T_{shell} + T_{mold})(T_{shell}^2 + T_{mold}^2) \tag{9}$$

where the Stefan-Boltzmann constant, σ_{SB} is $5.6704\times10^{-8}\mathrm{Wm^{-2}K^{-4}}$, ε_{shell} and ε_{mold} are the shell and the mold surface emissivities, taken to be 0.8; T_{shell} and T_{mold} are the surface temperatures. The heat transfer coefficient due to conduction is calculated with four resistances connected in series:

$$\frac{1}{h_{cond}} = \frac{1}{h_{mold}} + \frac{(d_{gap} - d_{slag})}{k_{air}} + \frac{d_{slag}}{k_{slag}} + \frac{1}{h_{shell}} \tag{10}$$

where the first resistance, $1/h_{mold}$, is for contact between the mold hot face surface and the solidified mold-slag layer; the next resistance is due to conduction through the local air layer, d_{gap}, calculated from the thermal-mechanical model displacement results. The third resistance is conduction through the slag layer, and the final resistance is a temperature-dependent contact resistance between the slag and the outer surface of the steel shell. The specific parameters for this resister model, given in Table 1, are taken mainly from (Meng and Thomas, 2003). These calculations are performed with CON1D and also calculated in the (ABAQUS, 2013) models via the GAPCON user subroutine.

Ferrostatic pressure in the liquid steel pool, that pushes the continuously solidifying shell towards the contact surfaces of the mold, is implemented into the solidifying steel shell model via the DLOAD subroutine as a distributed load which increases linearly with vertical distance (time) down the mold. This methodology is described in more detail by (Zappulla, 2016). Mechanical interaction between the shell and the mold contact surfaces is accounted for using coulomb friction with a friction factor of $\mu = 0.15$ based on measurements by (Meng et al., 2006). Sliding contact that permits gap formation without permitting penetration is enforced using the contact algorithm in ABAQUS with the mold hotface as the “master” surface and the shell exterior as the “slave” surface.

Table 1
CON1D interfacial gap parameters.

Interfacial gap parameter	Value	Unit
Solidification temperature of slag	1083	°C
Conductivity of slag	1.5	W/m·K
Contact resistance of slag layer/mold	5.0×10^{-9}	m^2·K/W
Dynamic viscosity of slag at 1300 °C	1.8	P
Exponent for temperature dependence of viscosity	0.9	-
Density of slag	2500	kg/m^3
Absorption factor of slag	250	1/m
Refraction index of slag	1.5	-
Emissivity of slag	0.9	-
Mold powder consumption rate	0.399	kg/m^2
Oscillation mark depth	0.324	mm
Oscillation mark width	1.5	mm
Mold oscillation frequency	2.5	cps
Mold oscillation stroke	6.6	mm
Ratio of solid slag velocity/casting speed (WF)	0.16	-
Ratio of solid slag velocity/casting speed (NF)	0.167	-

3. Viscoplastic model of solidifying steel

The total strain in this elastic-viscoplastic model is split into three components, written in rate form as:

$$\dot{\varepsilon} = \dot{\varepsilon}_{el} + \dot{\varepsilon}_{th} + \dot{\varepsilon}_{ie} \tag{11}$$

where tensors $\dot{\boldsymbol{\varepsilon}}_{\mathbf{el}}, \dot{\boldsymbol{\varepsilon}}_{\mathbf{th}}, \dot{\boldsymbol{\varepsilon}}_{\mathbf{ie}}$ contain the components of the elastic, thermal and inelastic (both rate-independent plascticity and rate-dependent creep) strain rates. The stress and strain rates then are related by the constitutive equations:

$$\dot{\boldsymbol{\sigma}} = \underline{\mathbf{D}}: (\dot{\boldsymbol{\varepsilon}} - \boldsymbol{\alpha}\dot{T} - \dot{\boldsymbol{\varepsilon}}_{\mathbf{ie}}) \tag{12}$$

where $\underline{\mathbf{D}}$ contains the isotropic elasticity constants based on the temperature-dependent elastic modulus and Poisson ratio, as given in (Koric and Thomas, 2008). The thermal strain term depends on the isotropic temperature-dependent thermal expansion $\boldsymbol{\alpha}$ coefficient tensor, found from the temperature-dependent density, as explained by (Koric and Thomas, 2006), and the evolving temperature distribution calculated from the transient thermal model results, T.

In case of finite deformation, the objective stress rate is provided by the Jaumann stress rate $\hat{\boldsymbol{\sigma}}$:

$$\hat{\boldsymbol{\sigma}} = \dot{\boldsymbol{\sigma}} + \boldsymbol{\sigma}: \mathbf{W} - \mathbf{W}:\boldsymbol{\sigma} \tag{13}$$

where $\mathbf{W}$ is the anti-symmetric part of the velocity gradient.

Even though there is no explicit yield condition, like in classical plasticity, inelastic effects are assumed to follow “J2 plasticity" with isotropic hardening. The inelastic strain rate $\dot{\boldsymbol{\varepsilon}}_{\mathbf{ie}}$ is found assuming the Prandtl-Reuss equations:

$$\dot{\boldsymbol{\varepsilon}}_{\mathbf{ie}} = \dot{\bar{\varepsilon}}_{\mathrm{ie}} \frac{3}{2} \frac{\boldsymbol{\sigma}'}{\bar{\sigma}} \tag{14}$$

where $\bar{\sigma}$is the effective or Von Mises stress:

$$\bar{\sigma} = \sqrt{\frac{3}{2}\boldsymbol{\sigma}': \boldsymbol{\sigma}'} \tag{15}$$

while $\boldsymbol{\sigma}'$ is a deviatoric stress tensor defined by:

$$\boldsymbol{\sigma}' = \boldsymbol{\sigma} - \frac{1}{3} p\mathbf{I} \tag{16}$$

and the pressure portion of the Cauchy stress tensor is:

$$\mathrm{p} = \frac{1}{3} tr(\boldsymbol{\sigma}) \tag{17}$$

Unified viscoplastic models treat creep and plasticity as a combined "inelastic strain", whose instantaneous rate of change depends on the current stress, temperature, and “structure”. Structure is represented by one or more scalar or tensor state variables, which evolve with time, and can include phenomena such as rate of phase transformation. (Lush et al., 1989) obtained traditional elastic-viscoplastic models when inelastic strain is selected as the structure parameter. Thus, the current model employs such a unified constitutive model, with inelastic strain as the single structure parameter. Here, inelastic strain rate $\dot{\bar{\varepsilon}}_{\mathrm{ie}}$ is related to stress, temperature, inelastic strain, and carbon content, %C:

$$\dot{\bar{\varepsilon}}_{ie} = f(\bar{\sigma},\ T,\ \bar{\varepsilon}_{ie},\ \%C) \tag{18}$$

Separate relations are used for each metallurgical phase: austenite, ferrite, and liquid.

3.1. Austenite constitutive model

For the austenite phase, a unified formulation proposed by (Kozlowski et al., 1992) is used, which matches both the creep test data of (Suzuki et al., 1988) and the tensile test data measured by (Wray, 1982):

$$\dot{\bar{\varepsilon}}_{ie}[\sec^{-1}] = f_C(\bar{\sigma}[MPa] - f_1\,\bar{\varepsilon}_{ie}|\bar{\varepsilon}_{ie}|^{f_2-1})^{f_3} \exp\left(-\frac{Q}{T[K]}\right)$$

where:
Q=44,465
$f_1 = 130.5\text{-}5.128 \times 10^{-3} T[K]$
$f_2 = \text{-}0.6289\text{+}1.114 \times 10^{-3} T[K]$
$f_3 = 8.132\text{-}1.54 \times 10^{-3} T[K]$
$f_C = 46{,}550 + 71{,}400(\%C) + 12{,}000(\%C)^2$ (19)

where Q is an activation energy constant, $\bar{\sigma}$ (MPa) is Von Mises effective stress, empirical functionsf_1, f_2, f_3, f_C depend on absolute temperature (K), and $\%C$ is carbon content (weight percent), which is one of the ways that steel grade (composition) is represented. (Li and Thomas, 2004) showed that Eqn. (19) allows an algorithmic approximation of kinematic hardening, where $\bar{\sigma}$ and $\dot{\bar{\varepsilon}}_{ie}$ are signed according to the largest principal stress and strain rate component respectively. They demonstrated reasonable agreement with some cyclic fatigue test data at high temperatures.

Originally fitted to tensile-test and creep data for plain carbon steel, Fig. 3 compares the Kozlowski model III constitutive equation with data points measured by (Wray, 1982) for plain carbon steel at two different temperatures. The form of this austenite constitutive model is rather restrictive to allow inclusion of realistic behavior during cyclic loading, such as kinematic hardening, and the Bauschinger effect.

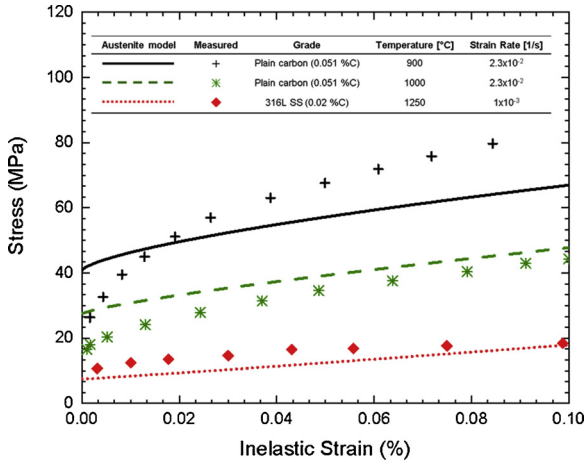

Fig. 3. Austenite constitutive model for plain carbon steel (Wray, 1982) compared with stainless steel data (Venugopal et al., 1993) (For interpretation of the references to colour in this figure legend, the reader is referred to the web version of this article).

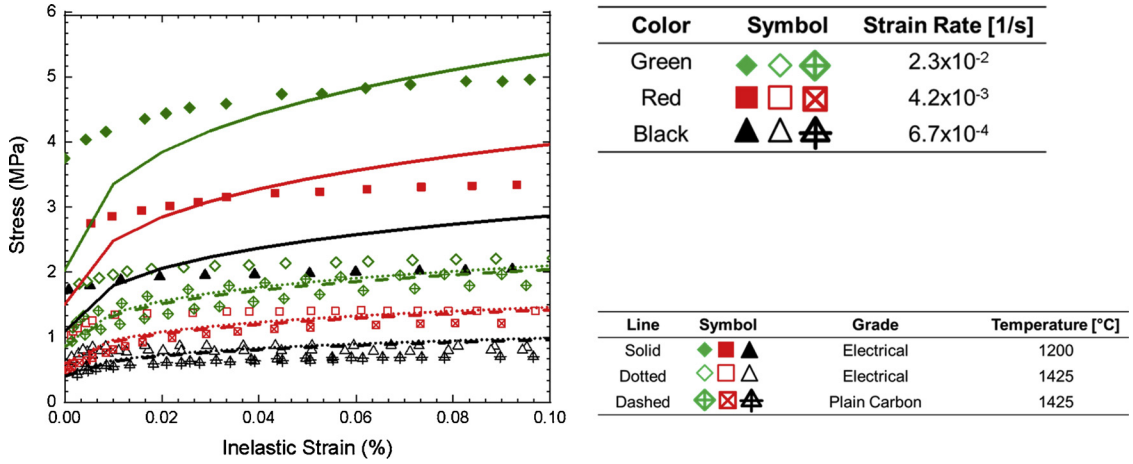

Fig. 4. Delta-ferrite constitutive model results for plain carbon steel (lines) compared with measurements (symbols) by (Wray, 1976) at 2 temperatures, and 3 strain rates, for two steel grades (For interpretation of the references to colour in this figure legend, the reader is referred to the web version of this article).

3.2. Ferrite constitutive model

For the δ-ferrite phase, a power law constitutive model proposed by (Zhu, 1996), is implemented, as given in Eqn. (20). This model was fitted to match tensile-test measurements of plain carbon steel made by (Wray, 1976).

$$\dot{\bar{\varepsilon}}_{ie}(1/\text{sec}) = 0.1\left|\frac{\bar{\sigma}(MPa)}{f_{\delta c}(\%\text{C})\left(\frac{T(^{o}K)}{300}\right)^{-5.52}(1+1000\bar{\varepsilon}_{ie})^{m}}\right|^{n}$$

where:

$$f_{\delta c}(\%C) = 1.3678 \times 10^{4}(\%C)^{-5.56\times10^{-2}}$$

$$m = -9.4156 \times 10^{-5}T(^{o}K) + 0.3495$$

$$n = \frac{1}{1.617 \times 10^{-4}T(^{o}K) - 0.06166} \quad (20)$$

Fig. 4 shows this ferrite model integrated within the relevant low strain range for a variety of constant temperatures and strain rates. For the same conditions, this phase is almost an order of magnitude weaker than austenite. As with the austenite model, the ferrite model is also restrictive to accommodate kinematic hardening and the Bauschinger effect in cyclic loading, which increases the difficulty of fitting the model accurately. Compositions for all steel grades discussed in this work can be found in Table 2.

3.3. Liquid and mushy phase constitutive model

Similar to the works of (Koric and Thomas, 2006) and (Zappulla et al., 2017), the liquid and mushy zones are modeled with an isotropic elastic-perfectly-plastic rate-independent constitutive model, using a small, constant yield stress of 0.01 MPa, whenever temperature exceeds the solidus temperature.

3.4. Phase based constitutive model selection

As different steel phases have greatly different mechanical properties, the choice of constitutive model in this work depends on the phase-fraction evolution with temperature of the particular steel grade of interest, and the transition between phases, as described by (Zappulla et al., 2017). In two-phase regions, most thermal and mechanical properties are modeled based on a simple weighted average summation based on phase fraction. Constitutive equations are handled differently.

In austenite/ferrite mixtures, the Zhu model for ferrite is applied in the solid when the ferrite volume fraction exceeds 10 %. Otherwise, the Kozlowski Eqn. (19) is used. This criterion was chosen over a mixture law based on phase fractions, because time-dependent inelastic response in the ferrite phase governs the local mechanical behavior if the ferrite domain is unbroken. The previous work of (Hibbeler and Thomas, 2011) found that a transition of 10 % matched quite well with a more complicated transitional model using an Eshelby tensor with multiple phases. Details on the method devised to integrate these highly nonlinear constitutive equations are explained in (Koric and Thomas, 2006), and were implemented via the UMAT subroutine in ABAQUS.

Fig. 5 shows the results of both constitutive models, integrated for the same conditions as data measured by (Venugopal et al., 1993) for 316L stainless steel. The austenite is observed to be about 10X stronger than the corresponding ferrite, and the Kozlowski model agrees with the measured data.

4. Phase-based material properties for stainless steel

The composition of steel greatly influences its mechanical properties. Due to the many different types of steel, comprehensive mechanical-property experimental-data for the range of high temperatures, low strains, and low strain rates of interest in casting processes is difficult to find for any given steel grade. Although plain carbon steels are defined by their carbon content, they also contain up to several weight percent of many other alloying elements, which depend heavily on the specific grade. Higher alloy steels such as next generation Advanced High-Strength Steels, tool steels, and stainless steels have substantially higher amounts of specific alloying elements (such as Si, Mn, Cr, and Ni) in order to achieve specific enhanced properties such as ductility-to-strength ratio, hardenability, hot working strength, and corrosion

Table 2
Compositions (wt.%) of steel grades used in the present work.

Steel grade	C	Mn	Si	S	P	Cr	Ni	Al	Ti	N
Plain Carbon 1 (Wray, 1982)	0.051	0.82	0.28	0.018	0.001	-	-	< 0.002	-	0.001
Plain Carbon 2 (Wray, 1976)	0.028	0.01	0.006	0.004	0.001	-	-	0.001	-	0.001
Electrical (Wray, 1976)	0.017	0.01	3.01	0.004	0.001	-	-	0.002	-	0.003
316L SS (Venugopal et al., 1993)	0.02	1.7	0.77	0.007	0.04	18.2	11.6	-	-	-
409L SS	0.005	0.27	0.54	0.001	0.0224	11.2	0.1	0.003	0.22	0.008

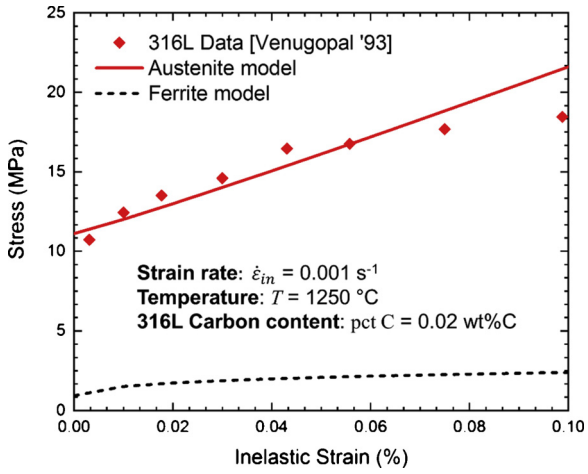

Fig. 5. Constitutive models of austenite and ferrite for 316L stainless steel with experimental data (Venugopal et al., 1993).

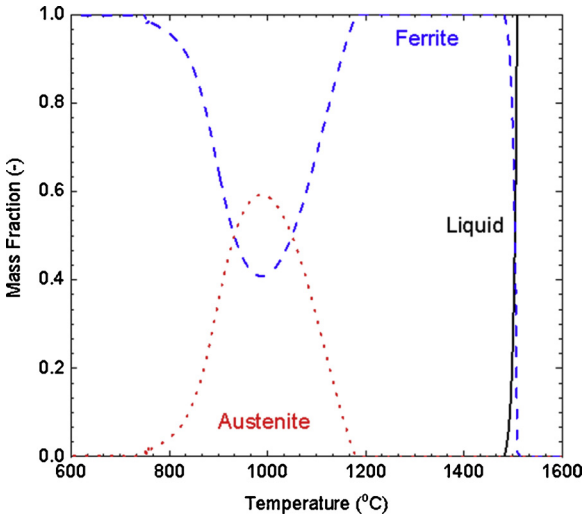

Fig. 6. Phase fractions for 409L stainless steel.

resistance.

Originally fit to data for specific plain carbon steels, both the austenite and ferrite models of the Kozlowski-Zhu constitutive laws exhibit good agreement with tensile-test data for other types of steel when the temperature, strain rate, and phase evolution are the same. Fig. 3 in section 3.1, which shows the austenite constitutive model and some of its plain-carbon fitting data, also compares the predictions of this model with tensile-test measurements for 316L stainless steel obtained by (Venugopal et al., 1993) at the appropriate temperature and strain rate. As also shown in Fig. 5, the agreement is remarkable and significant, considering the very different composition of this steel. Furthermore, Fig. 4 in section 3.2, which shows the δ-ferrite constitutive model and some of its fitting data, also compares the predictions of this model with tensile-test measurements for a high-silicon electrical steel, which falls in the ferrite regime. Again, a very close fit is obtained for this very different steel grade.

Very little mechanical property data can be found for specific steels at elevated temperatures. High temperature stress-strain data for the temperature-, strain-, and strain-rate conditions encountered during continuous casting for 409L could not be found in the literature. However, while high temperature steel properties depend on composition, the specific phase at a given temperature is substantially more relevant to its behavior as shown by the results presented above. Therefore, finding the proper phase diagram, more specifically the phase fraction history of a given steel grade, and using phase specific constitutive equations is a sufficient and more convenient method for determining mechanical behavior during solidification, without the necessity of performing complete mechanical testing in this regime. This method has been previously validated by (Rowan et al., 2011) comparing predictions using the Kozlowski-Zhu constitutive laws with force measurements in solidifying steel shells. Other similar studies, including those by (Koric et al., 2010a) and (Zappulla and Thomas, 2017) have applied this approach to investigate various aspects of the continuous casting process.

As with all steels, stainless steels can exhibit a wide range of thermal and mechanical properties during solidification. The steel of interest in this work, 409L, is a specific type of ferritic stainless steel. Stainless steels as a group are designed to withstand corrosive environments, due to high chromium and nickel contents, which help to create a strong protective oxide layer adhered tightly to the surface. These higher alloy contents also strongly affect phases as well as micro constituents, and depending upon the exact chemical composition of the steel, the high-temperature microstructure during casting may consist of austenite, ferrite, or a mix of the two phases.

Based on its composition shown in Table 2, the evolution of the volume fractions of each phase with temperature during solidification and cooling of 409L stainless steel are shown in Fig. 6, calculated from the appropriate multi-dimensional equilibrium phase diagram based on free-energy minimization with JMatPro (Senta Software Ltd., 2016). Specific transformation temperatures are given in Table 3.

Compared to plain carbon steel grades, the phase history of 409L stainless has substantially different austenite and ferrite regions. Whereas in plain low-carbon steels, solidification to δ-ferrite is followed by complete transformation into austenite, in this particular ferritic stainless steel, ferrite is still stable all the way to room temperature. Fig. 6 shows that the cooling steel only partially transforms into austenite, reaching a maximum austenite fraction of about 60 % at ~1000 °C, followed by a complete transition back into ferrite.

The temperature-dependent thermal properties: conductivity and enthalpy, shown in Fig. 7, are calculated by JMatPro (Senta Software Ltd., 2016) and input into ABAQUS subroutines. The temperature-dependent elastic modulus, density, and thermal linear expansion are shown in Fig. 8.

Decreasing temperature leads to increases in density and elastic modulus as the crystal structure become more tightly packed and stiffer. In addition, as the steel changes phase from ferrite to austenite, and thus from body-centered-cubic to close-packed face-centered-cubic, the atomic packing fraction also increases, so the density further increases, as the lattice spacing becomes smaller.

This is accompanied by corresponding decreases in the thermal linear expansion, which is inversely related to the cube root of the density at a given temperature.

5. Results and discussion

5.1. Multiphysics model of stainless-steel slab caster

The coupled multiphysics model, including the Kozlowski-Zhu constitutive laws, was employed to quantify the thermo-mechanical

Table 3
Transition temperatures for 409L stainless steel.

Stainless Steel 409L	
Pour temp.	1555.00 °C
Liquidus temp.	1508.63 °C
Solidus temp.	1481.93 °C
Mushy zone	26.7 °C
Austenite start	1180 °C
Austenite end	753 °C

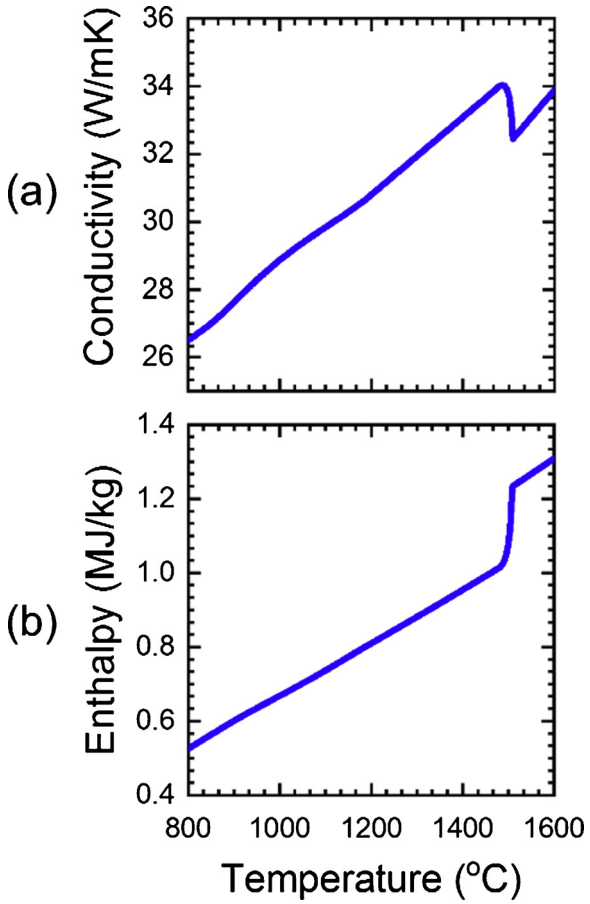

Fig. 7. Thermal properties of 409L stainless steel: (a) conductivity and (b) enthalpy.

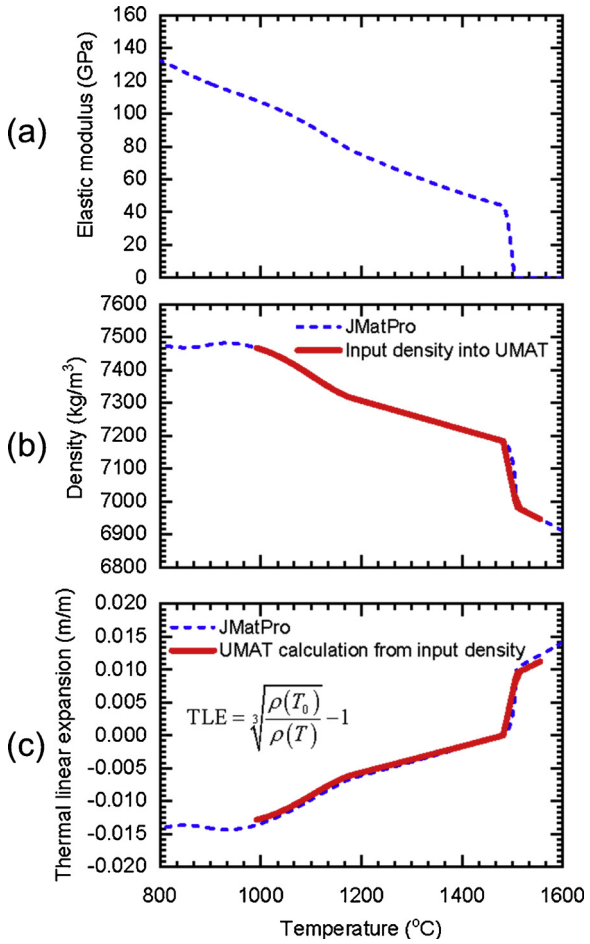

Fig. 8. Mechanical properties of 409L stainless steel: (a) elastic modulus, (b) density, (c) thermal linear expansion.

nature of solidifying 409L stainless steel in a commercial continuous slab caster with a 220 mm (thickness) x1260 mm (width) strand, cast at 1 m/min casting speed in a straight mold with a working length of 0.8 m and 120 mm nozzle submergence depth. The slice domain of the shell model in Fig. 2 begins at the meniscus, with a uniform pouring temperature, and no initial displacement, strain, or stress. The 2D domain is discretized with ~24,000 four-node, temperature-displacement generalized plane-strain elements, providing an average element size (0.3 mm) – which is sufficient to capture thermo-mechanical solidification phenomena on a fixed grid according to (Zappulla et al., 2017). The 1D domain has a uniformly refined mesh of 0.1 mm square elements. The "slice" model approach is justified for the heat transfer analysis, due to insignificant axial (casting direction) conduction compared to heat advected by the casting velocity, i.e. large Péclet number. (Li and Thomas, 2004) and later (Koric et al., 2010a) have found that generalized plane strain, with constant axial strain and negligible out of plane bending, is capable of reproducing the complete 3D stress state in continuous casting modeling, and is therefore applied as a suitable 2D mechanical approximation in this work as well.

5.2. Thermal flow in liquid pool

Fig. 9 shows time-averaged flow patterns and temperature distributions in the liquid steel at horizontal and center-middle planes in the mold, calculated from the 3D turbulent thermal fluid flow model. Owing to the lower casting speed of stainless-steel casters, (relative to typical plain-carbon steel casters), the jet is angled upward (5° up), in order to increase surface velocity into an optimum range for good steel quality reviewed by (Dauby, 2012).

The distribution of superheat is governed by the flow pattern in the mold region. The jet flowing from the nozzle traverses the mold interior to impact upon the narrow faces, transferring most of the superheat to the solidifying steel shell on the narrow faces. The jet then separates to flow upward towards the top surface and down the narrow faces deep into the strand. The temperature of the flowing steel continuously drops as superheat is removed at the solidification front, so the stagnant regions in the center of the lower recirculation zones are coldest.

The mold flow causes an uneven distribution of superheat flux, showing a peak at a region in the middle of the narrow face and 200 mm below meniscus, as shown in Fig. 10. The superheat flux delivered to the solidification front at the wide faces is observed in this figure to be much smaller.

The heat flux removed from the outer surface of the solidifying shell, across the interfacial gap and into the mold, is naturally much larger than the superheat flux, and depends on the difference between the calculated mold-wall shape and the shrinking steel-shell size.

5.3. Heat flux in the mold and model validation

Measurements were obtained from the operating caster to enable calibration and validation of the heat transfer model. This includes the measured heatup of the cooling water between entering and leaving the mold wide faces and narrow faces and the measured temperatures from thermocouples in the mold walls during ~3 hours of nearly steady casting in the real plant. Fig. 11 shows time histories of average heat flux leaving the mold, which are calculated from the water heatup, knowing the water flow rate, and the total mold surface area. The time averages of these heat fluxes are also given.

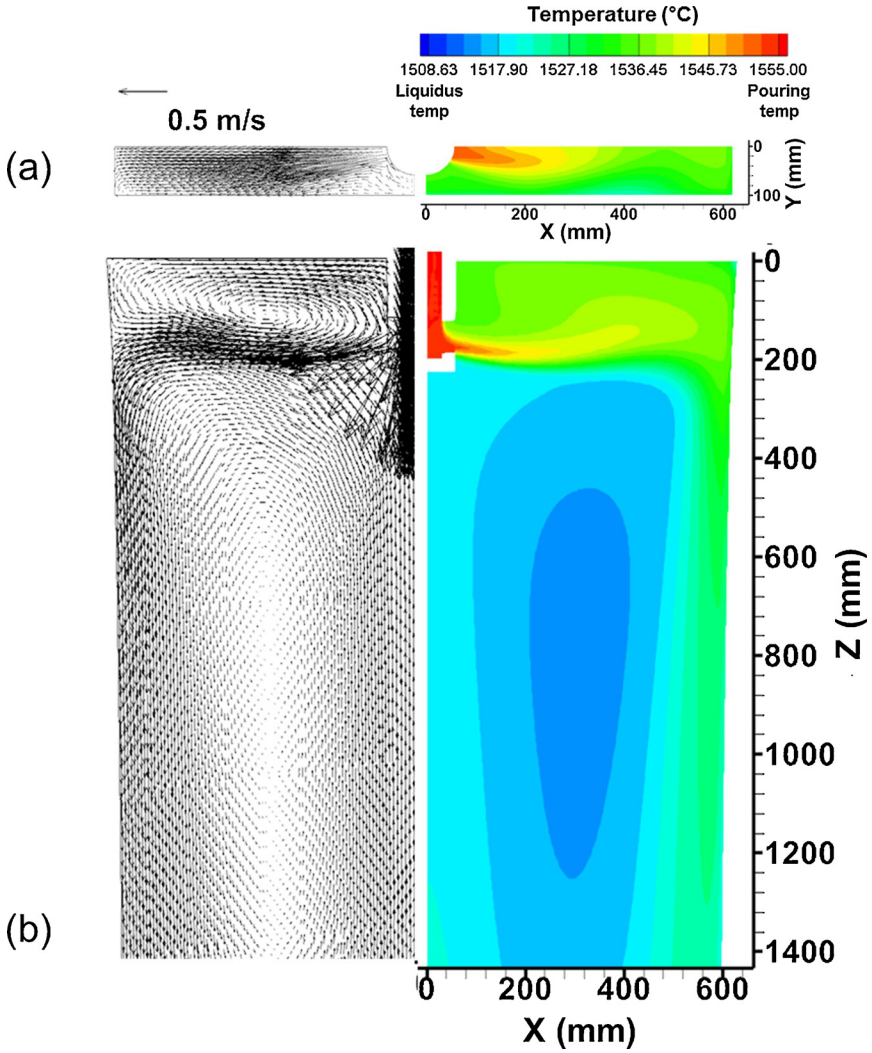

Fig. 9. Molten-steel flow patterns and temperature distributions at (a) horizontal plane 180 mm below the meniscus and (b) center plane between the wide faces in the mold.

Fig. 12 shows plant measurements from 13 thermocouples (TCs) located 110 mm below the meniscus, and 20 mm beneath the mold hot face. The time- and spatial- averages of these temperature histories are also included in Fig. 12(b). The thermocouple data of TCs 4-10 located in the central wide face region away from the corners average 120.4 °C with standard deviation of 3.7 °C.

The average heat flux across the interface between the steel shell and the mold hot face predicted by the CON1D model, is calculated by integrating the interface heat flux profile along the casting direction, shown in Fig. 10, and dividing by the total mold length (900 mm) and width. These calculated average heat fluxes agree reasonably with the measurements: WF: 1.10 (predicted) vs. 1.24 (measured) MW/m^2 and NF: 1.15 (predicted) vs. 1.25 (measured) MW/m^2. Furthermore, the temperature in the mold wide face predicted at the thermocouple location exactly matches the measured average thermocouple data, as shown in Fig. 13. Matching both average mold heat flux and thermocouple temperatures in the upper mold is significant because it suggests that the entire heat flux profile cannot be too far from reality. This was achieved by careful adjustment of model thermal parameters in Table 1 such as the ratio of solid slag velocity/casting speed.

The non-uniform superheat distributions, caused by the mold flow pattern, results in local thinning and temperature variations in the solidifying steel shell which greatly affects thermal stress behavior in the shell, and quality of the final steel products. As described previously, the superheat profile on the narrow-face centerline is higher than on the wide face, which makes the shell thickness of the narrow face substantially thinner than the wide face, as shown in Fig. 14. This is also influenced by heat transfer through the interfacial gap between the steel shell and mold contact surface. Fig. 13 shows that the shell surface temperature starts to decrease faster at ~400 mm below the meniscus, which is accompanied by corresponding decreases in slope of the mold wall temperatures. This is due to decreasing gap thickness, from better contact between the steel shell and the mold surfaces at that location. The model predictions of both shell thickness and mold temperature profiles are quantitatively verified by comparing the models (CON1D and ABAQUS), in addition to the validation of CON1D with plant measurements already discussed.

5.4. Stress and deformation in solidifying steel shell

Fig. 15 shows temperature and hoop stress profiles down the surface of the wide face and narrow face in the mold. The hoop stress acts tangentially to the surface around the strand circumference. Note that the hoop stress directions are different for the two mold faces in the global coordinate system (ie x direction on WF and y direction on NF). Both locations experience similar but slightly different temperature histories, with the wide face dropping to a lower temperature by mold exit, while the narrow face remains hotter as a result of the higher

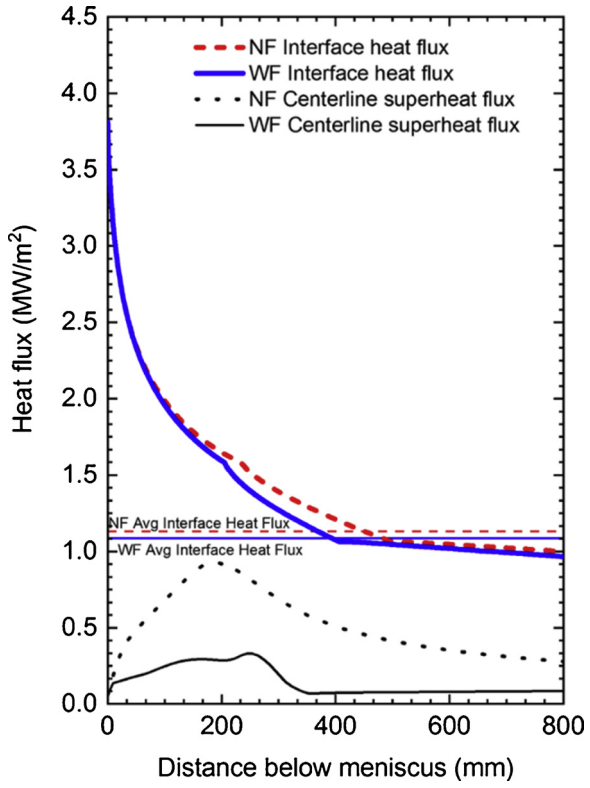

Fig. 10. Calculated interfacial and superheat flux profiles down mold centerlines.

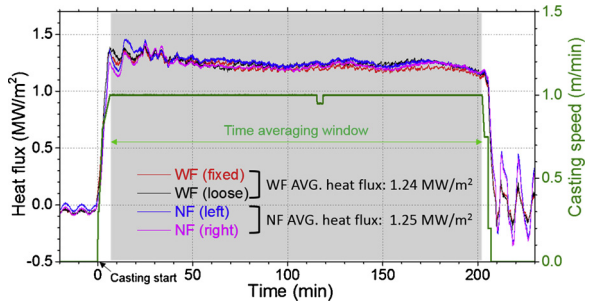

Fig. 11. Heat flux measurements from heatup of mold cooling water.

superheat flux from the liquid. Stress results are qualitatively similar with both locations experiencing two tensile stress peaks. The first peak is initiated from the rapid shrinkage associated with the phase transformation from ferrite to austenite. The second peak is due to the small but sudden increase in cooling rate at the surface as a result of renewed contact with each respective mold wall. The delay in the compression of the narrow face is due to its higher temperature, and after a longer time, the surface stress there also drops back into compression.

Fig. 16 gives hoop stress results through the shell thickness at various times during solidification. The expected thermo-mechanical behavior for plain carbon steel, observed by several previous researchers including (Zappulla et al., 2017), is compression at the chilled surface, transitioning into tension towards the solidification front, and then to nearly zero (the ferrostatic pressure) in the liquid. This behavior is also seen in the analytical solution of thermal stress during solidification of a single-phase material by (Weiner and Boley, 1963). In addition, a tensile peak often appears at the surface at early times when the cooling rate is high. The new stainless steel results generally exhibit both of these behaviors. However, as discussed previously and shown in Fig. 15, a secondary tensile peak appears at the surface, at later times. Another second tensile peak is also seen to appear inside the shell near the solidification front, moving further beneath the surface with time (Fig. 16).

Fig. 17 shows a single snapshot of hoop stress through the thickness at 60 s below the meniscus of the wide face centerline, using the refined-mesh slice model. This snapshot also includes the phase fractions, in order to understand the stress profile. The difference between the classic behavior of plain carbon steels, surface compression and subsurface tension, is a second compression peak, which is explained by some austenite transforming back into ferrite between 3 and 8 mm beneath the surface, as shown in the inlaid plot of the austenite and ferrite phase fractions. The region transforming back into ferrite experiences an expansion from a FCC to BCC crystal structure, and is forced into compression by the surrounding stronger material: the austenite-rich region on the inside, and the ferrite region at the surface (which becomes much stronger at the lower temperatures). This new compression peak divides the usual subsurface tensile region into two stress peaks. The first interior peak coincides with the maximum phase fraction of austenite (the stronger phase) and the second is generated within the δ-ferrite region due the cooling (compressive) surface region.

These results show that differences in phase transformations between steel grades have a great effect on their stress evolution during solidification. In addition, changes in surface cooling rate are observed to have an equally-important effect on stress evolution at the surface. When considered together with the work by (Zappulla et al., 2017) on the grade effects in plain-carbon steels during solidification, the mechanical behavior of solidifying steels becomes more clear.

Fig. 18 shows the deformed shell and its temperature contours at various times in the mold, calculated using the L-shaped domain, (Fig. 2). The shell contracts and shrinks away from the mold most at the corner region, which has the lowest temperatures due to 2D heat transfer and is strong enough to support the internal ferrostatic pressure. Similar corner behavior is reported in many previous works such as by (Li and Thomas, 2004) and subsequently by (Koric et al., 2010a). Shrinkage of the wide-face shell is more than the narrow-face mold taper can compensate within ~100 mm below the narrow face meniscus, (Fig. 18a), and near mold exit, (Fig. 18d), so bulging is often experienced at those locations. Such bulging can lead to surface depressions, cracks and other problems below the mold, as explained previously by (Thomas et al., 1996) followed by (Li and Thomas, 2002). Improved taper design of the narrow faces, as suggested by (Thomas and Ojeda, 2003) can help lessen these problems.

5.5. Computational considerations

Combined nonlinearities from the highly nonlinear material response, coupled distribution of superheat from the CFD model, and complex boundary and contact conditions between the shell and mold lead to significant ill-conditioning of the coupled thermo-mechanical global finite element stiffness matrix. ABAQUS uses the Newton-Raphson method to bring the system of nonlinear finite-element equations into equilibrium within each quasi-static increment. The direct multi frontal solver, used to solve linearized equations in ABAQUS/standard, is parallelized with the hybrid MPI/OpenMP implementation. The 150,000 DOF thermo-mechanical model took several days on 4 nodes (96 cores) of the 2016 iForge system at NCSA to reach 48 s of total simulation time down the mold length. The CFD and 3D Mold calculations were larger, but with fewer nonlinearities and better parallel scalability on HPC.

(Koric and Gupta, 2016) have recently benchmarked a similar multi-frontal solver on a large supercomputer, and effectively scaled the solution time on several thousand processors. This shows that the accurate modeling of multiphysics solidification problems, such as presented in this work, is becoming increasingly feasible, using high performance, parallel computing resources.

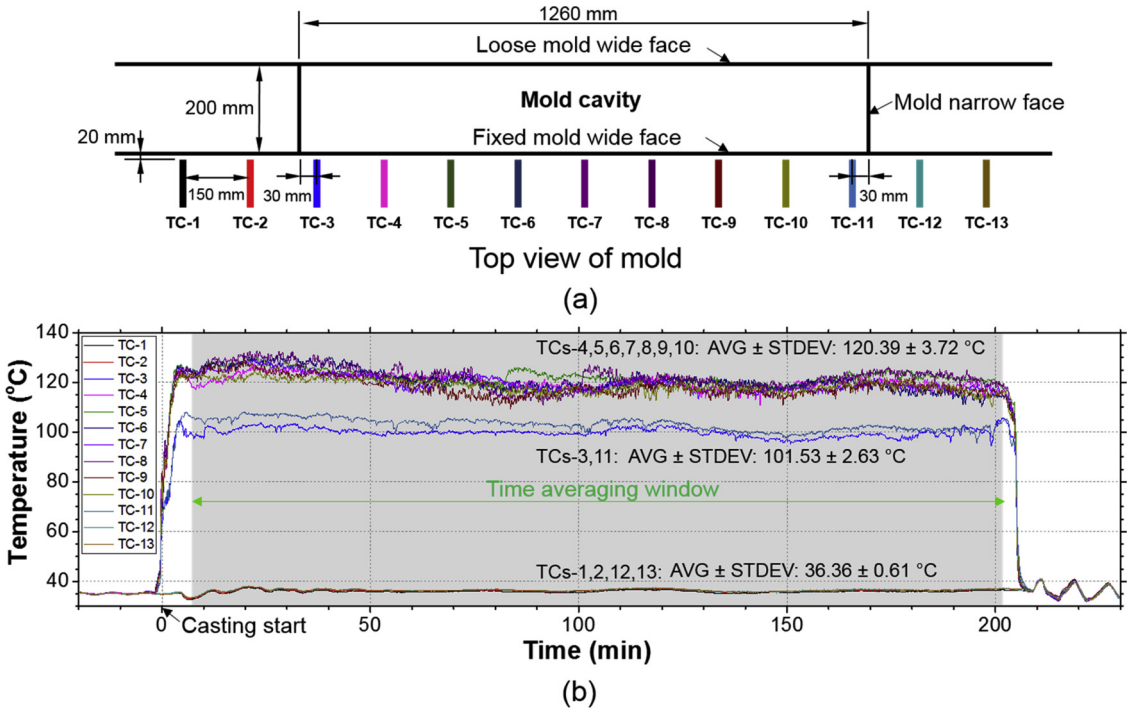

Fig. 12. Thermocouple measurements: (a) locations and (b) temperature histories of thermocouples inserted on the mold wide face.

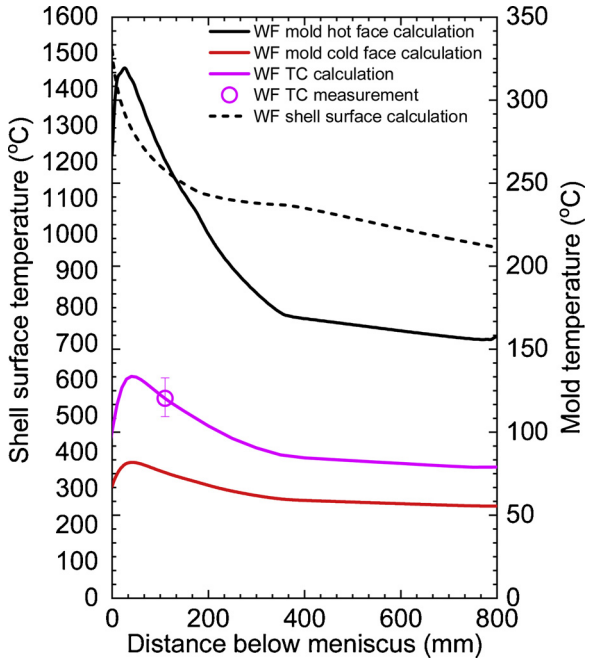

Fig. 13. Calculated mold and shell temperature results (wide face) with thermocouple validation.

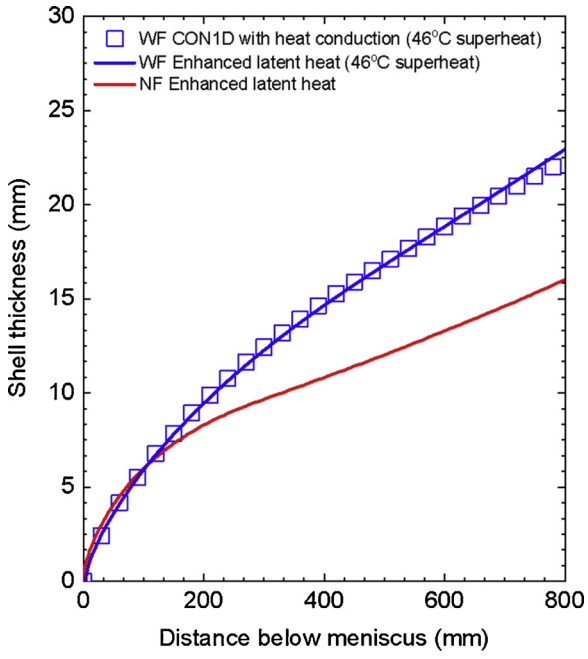

Fig. 14. Shell thickness results from CON1D and ABAQUS.

6. Conclusions

A multiphysics model for the study of stainless steel alloy solidification processes has been developed, which features phase-dependent constitutive equations. Specifically, the thermo-mechanical behavior of a solidifying stainless-steel shell in a straight-walled continuous casting mold is simulated using thermo-elastic-viscoplastic constitutive models for the austenite, ferrite, and liquid phases during the solidification process, which are tightly coupled with phase fraction calculations, as well as with highly nonlinear temperature-dependent properties.

These constitutive equations, which were originally fitted from data for plain carbon steel, are shown to reproduce tensile-test measurements for stainless steels as well, so long as the phase, temperature, and strain rate are the same. While high temperature steel properties depend greatly on composition, the specific phase at a given temperature is the reason for this behavior. Using phase-specific constitutive equations is a sufficient and more convenient method to determine mechanical behavior of solidifying steel without the need for complete mechanical testing data in this difficult regime.

The simulation results show that the stresses arising during solidification of a 409L ferritic stainless steel shell include a second subsurface compression peak through the shell thickness, due to the late

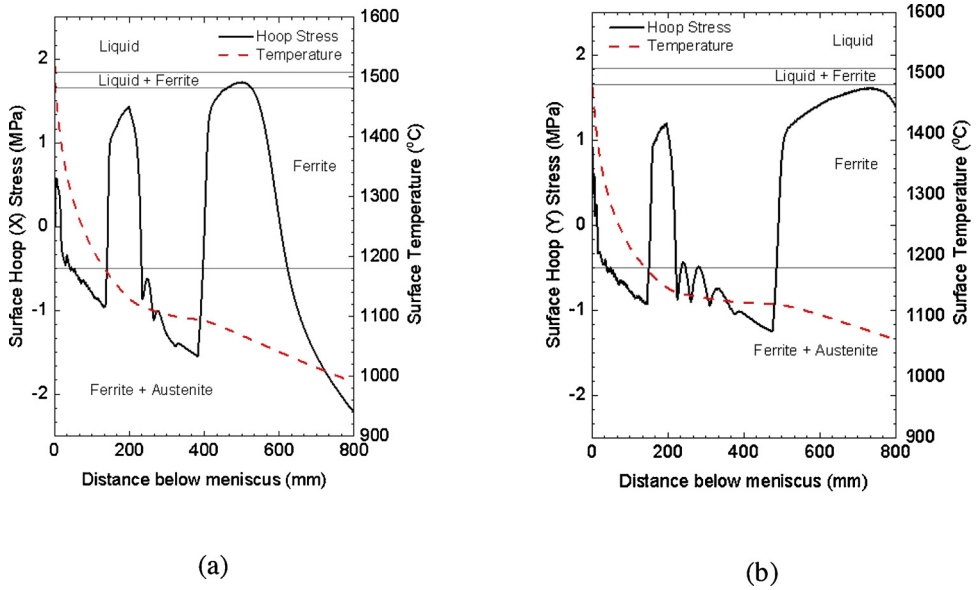

Fig. 15. Surface temperature and hoop stress results with superheat flux: (a) Wide face and (b) Narrow face.

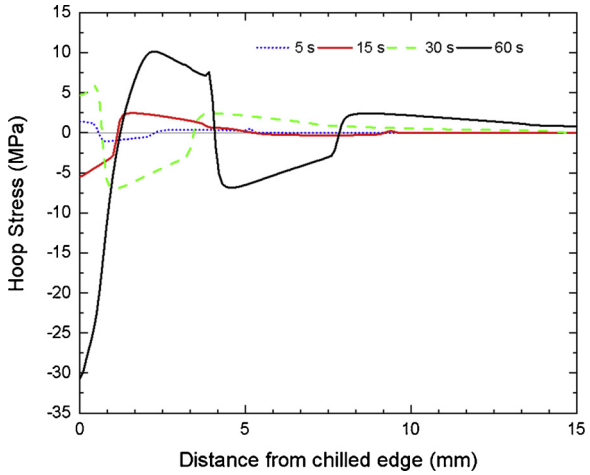

Fig. 16. Hoop stress profile through the thickness at different times below meniscus (WF centerline from slice model).

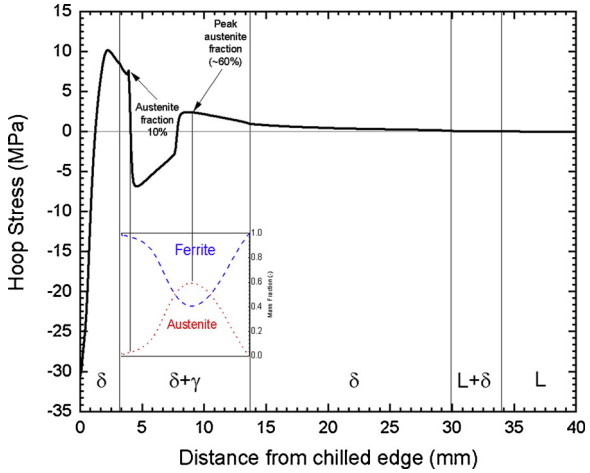

Fig. 17. Hoop stress and phase profile through the thickness 60 s below the meniscus (WF centerline from slice model).

phase change expansion from γ-austenite back to δ-ferrite, which is not seen in plain carbon steel. In addition to the phase change peak, it is found that abrupt changes in heat transfer, such as produced in this example by increases in the size of the evolving the shell/mold gap, and by the turbulent fluid flow, also lead to spikes in tensile stresses at the surface. This multiphysics model can predict the evolving temperature distribution, shrinkage, shape and stress during solidification of steel for different compositions, including stainless steel. It can be used to better understand the fluid flow and thermo-mechanical behavior, and to optimize the continuous casting process, such as by providing ideal mold taper profiles to minimize the formation of defects such as depressions, hot spots and cracks.

7. Future work

More work is needed to apply and couple additional physical phenomena into more comprehensive modeling systems, designed for a particular industrial solidification process of interest. While it is clear that the phase-dependent constitutive behavior approach demonstrated here is a valid method for handling these different steel grades, as newer advanced high strength steels grow in interest, more experimental measurements of mechanical behavior are needed to confirm this finding. Specifically, more tensile tests, creep tests, and reverse loading tests are needed in the high temperature, low strain, and low strain rate regimes experienced by these materials in commercial solidification processes. Finally, with the additional effort, multiphysics models such as this one will become increasingly valuable tools to understand how defects form, and to optimize solidification processes, such as stainless-steel continuous casting.

Acknowledgements

The authors thank the National Center for Supercomputing Applications (NCSA) Industry Program at the University of Illinois and its Blue Waters project funded by the National Science Foundation (NSF) and the State of Illinois as well as support from the Continuous Casting Center at the Colorado School of Mines, the Continuous Casting Consortium at University of Illinois at Urbana-Champaign, and two NSF GOALI grants (Grants No. CMMI-13-00907 and CMMI 18-08731). Financial support (Grant No. 4.0012983) and assistance in collecting plant data from POSCO are gratefully acknowledged. The ANSYS Inc. academic partnership program for providing Fluent licenses is also

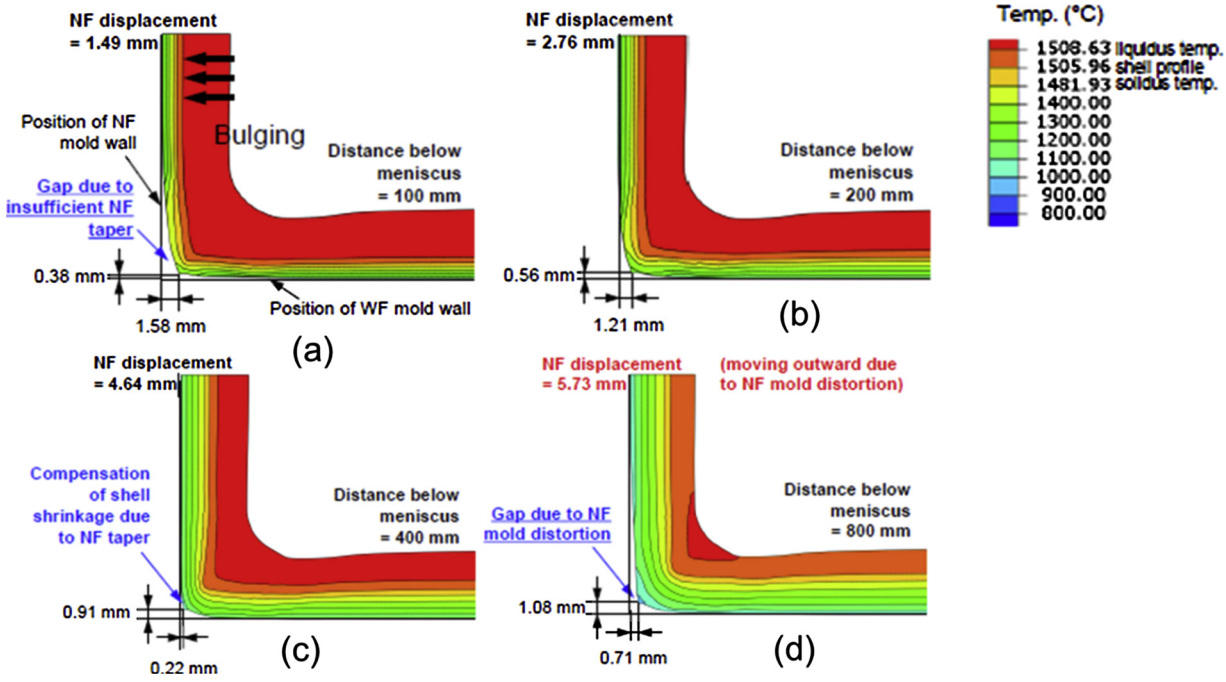

Fig. 18. Deformed shape with temperature contours: (a) 100 mm, (b) 200 mm, (c) 400 mm, and (d) 800 mm below meniscus.

appreciated.

References

ABAQUS, 2013. ABAQUS 6.13 Documentation Collection. DS SIMULIA Corp, Providence, RI.

Anand, L., 1982. Constitutive Equations for the Rate-Dependent Deformation of Metals at Elevated Temperatures. J. Eng. Mater. Technol. 104, 12. https://doi.org/10.1115/1.3225028.

ANSYS, 2012. ANSYS FLUENT 14.5-Theory Guide. ANSYS Inc., Canonsburg, PA., USA.

Bertelli, F., Faria, J.D., Goulart, P.R., Brito, C., Cheung, N., Garcia, A., 2016. Numerical and experimental modelling of two-dimensional unsteady heat transfer during inward solidification of square billets. Applied Thermal Engineering 96, 454–462. https://doi.org/10.1016/j.applthermaleng.2015.11.121.

Celentano, D.J., 2002. A thermomechanical model with microstructure evolution for aluminium alloy casting processes. International Journal of Plasticity. https://doi.org/10.1016/S0749-6419(01)00075-4.

Cheung, N., Santos, N.S., Quaresma, J.M.V., Dulikravich, G.S., Garcia, A., 2009. Interfacial heat transfer coefficients and solidification of an aluminum alloy in a rotary continuous caster. Int. J. Heat Mass Transf 52, 451–459. https://doi.org/10.1016/j.ijheatmasstransfer.2008.07.003.

Dantzig, J.A., Tucker III, C.L., 2001. Modeling in Materials Processing, first ed. Cambridge University Press, Cambridge, UK, pp. 106–118.

Dauby, P.H., 2012. Continuous casting: make better steel and more of it!. Revue de Metallurgie 109, 113–136. https://doi.org/10.1051/metal/2012011.

Groza, J.R., Shackelford, J.F., Lavernia, E.J., Powers, M.T., 2007. Materials Processing Handbook, first ed. CRC Press, Boca Raton, pp. 27–35. https://doi.org/10.1201/9781420004823.

Hibbeler, L.C., Thomas, B.G., 2011. Micromechanical Model for the Delta Ferrite-to-Austenite Transition. CCC Report, Urbana, Illinois.

Hibbeler, L.C., Thomas, B.G., Schimmel, R.C., Abbel, G., 2012. The thermal distortion of a funnel mold. Metall. Mater. Trans. B 43B, 1156–1172. https://doi.org/10.1007/s11663-012-9696-5.

Huespe, A.E., Cardona, A., Nigro, N., Fachinotti, V., 2000. Visco-plastic constitutive models of steel at high temperature. J. Mater. Process. Technol. 102, 143–152. https://doi.org/10.1016/S0924-0136(00)00442-8.

Inoue, T., Ju, D.Y., 1992. Analysis of solidification and viscoplastic stresses incorporating a moving boundary: an application to simulation of the centrifugal casting process. J. Therm. Stress. 15, 109–128. https://doi.org/10.1080/01495739208946124.

Koric, S., Thomas, B.G., 2006. Efficient thermo-mechanical model for solidification processes. Int. J. Numer. Methods Eng. 66, 1955–1989. https://doi.org/10.1002/nme.1614.

Koric, S., Thomas, B.G., 2008. Thermo-mechanical models of steel solidification based on two elastic visco-plastic constitutive laws. J. Mater. Process. Technol. 197, 408–418. https://doi.org/10.1016/j.jmatprotec.2007.06.060.

Koric, S., Hibbeler, L.C., Thomas, B.G., 2009. Explicit coupled thermo-mechanical finite element model of steel solidification. Int. J. Numer. Methods Eng. 78, 1–31. https://doi.org/10.1002/nme.2476.

Koric, S., Hibbeler, L.C., Liu, R., Thomas, B.G., 2010a. Multiphysics Model of Metal Solidification on the Continuum Level. Numer. Heat Transf. Part B Fundam. 58, 371–392. https://doi.org/10.1080/10407790.2011.540954.

Koric, S., Thomas, B.G., Voller, V.R., 2010b. Enhanced Latent Heat Method to Incorporate Superheat Effects into Fixed-Grid Multiphysics Simulations. Numer. Heat Transf. Part B Fundam. 57, 396–413. https://doi.org/10.1080/10407790.2010.496657.

Koric, S., Gupta, A., 2016. Sparse matrix factorization in the implicit finite element method on petascale architecture. Comput. Methods Appl. Mech. Eng. 302, 281–292. https://doi.org/10.1016/j.cma.2016.01.011.

Kozlowski, P.F., Thomas, B.G., Azzi, J.A., Wang, H., 1992. Simple constitutive equations for steel at high temperature. Metall. Mater. Trans. A 23, 903–918. https://doi.org/10.1007/BF02675567.

Kristiansson, J.O., 1982. Thermal stresses in the early stage of solidification of steel. J. Therm. Stress. https://doi.org/10.1080/01495738208942153.

Launder, B.E., Spalding, D.B., 1974. The numerical computation of turbulent flows. Comput. Methods Appl. Mech. Eng. 3, 269–289. https://doi.org/10.1016/0045-7825(74)90029-2.

Lee, J.-E., Yeo, T.-J., Hwan, O.K., Yoon, J.-K., Yoon, U.-S., 2000. Prediction of cracks in continuously cast steel beam blank through fully coupled analysis of fluid flow, heat transfer, and deformation behavior of a solidifying shell. Metall. Mater. Trans. A 31, 225–237. https://doi.org/10.1007/s11661-000-0067-5.

Li, C., Thomas, B.G., 2002. Maximum casting speed for continuous cast steel billets based on sub-mold bulging computation. 85th Steelmaking Conference Proceedings. Iron and Steel Society, Warrendale, PA, pp. 109–130.

Li, C., Thomas, B.G., 2004. Thermomechanical finite-element model of shell behavior in continuous casting of steel. Metall. Mater. Trans. B 35B, 1151–1172. https://doi.org/10.1007/s11663-004-0071-z.

Lush, A.M., Weber, G., Anand, L., 1989. An implicit time-integration procedure for a set of internal variable constitutive equations for isotropic elasto-viscoplasticity. Int. J. Plast. 5, 521–549. https://doi.org/10.1016/0749-6419(89)90012-0.

Meng, Y., Thomas, B.G., 2003. Heat-transfer and solidification model of continuous slab casting: CON1D. Metall. Mater. Trans. B 34, 685–705. https://doi.org/10.1007/s11663-003-0040-y.

Meng, Y., Thomas, B.G., Polycarpou, A.A., Prasad, A., Henein, H., 2006. Mould Slag Property Measurements To Characterize Cc Mould – Shell Gap Phenomena. Can. Metall. Q. 45, 79–94. https://doi.org/10.1179/000844306794409129.

Palumbo, G., Piccininni, A., Piglionico, V., Guglielmi, P., Sorgente, D., Tricarico, L., 2015. Modelling residual stresses in sand-cast superduplex stainless steel. J. Mater. Process. Technol. 217, 253–261. https://doi.org/10.1016/j.jmatprotec.2014.11.006.

Paquet, D., Dondeti, P., Ghosh, S., 2011. Dual-stage nested homogenization for rate-dependent anisotropic elasto-plasticity model of dendritic cast aluminum alloys. Int. J. Plast. 27, 1677–1701. https://doi.org/10.1016/j.ijplas.2011.02.002.

Pierer, R., Bernhard, C., Chimani, C., 2005. Evaluation of common constitutive equations for solidifying steel. Berg huettenmaenn monatsh 150 (5), 163–169. https://doi.org/10.1007/BF03165316.

Qin, Q., Tian, M., Pu, J., Huang, J., 2018. Constitutive investigation based on the time-hardening model for AH36 material in continuous casting process. Advances in Mechanical Eng. 10 (1), 1–11. https://doi.org/10.1177/1687814017750680.

Rowan, M., Thomas, B.G., Pierer, R., Bernhard, C., 2011. Measuring mechanical behavior of steel during solidification: Modeling the SSCC test. Metall. Mater. Trans. B 42B, 837–851. https://doi.org/10.1007/s11663-010-9470-5.

Safari, A.R., Forouzan, M.R., Shamanian, M., 2013. Thermo-viscoplastic constitutive

equation of austenitic stainless steel 310s. Comput. Mater. Sci. 68, 402–407. https://doi.org/10.1016/j.commatsci.2012.10.039.
Şahin, H.M., Kocatepe, K., Kayıkcı, R., Akar, N., 2006. Determination of unidirectional heat transfer coefficient during unsteady-state solidification at metal casting–chill interface. Energy Convers. Manag 47, 19–34. https://doi.org/10.1016/j.enconman.2005.03.021.
Senta Software Ltd, 2016. JMatPro. Guildford, United Kingdom.
Suzuki, T., Tacke, K.-H., Wuennenberg, K., Schwerdtfeger, K., 1988. Creep properties of steel at continuous casting temperatures. Ironmak. Steelmak. 15, 90–100.
Teskeredžić, A., Demirdžić, I., Muzaferija, S., 2002. Numerical Method For Heat Transfer, Fluid Flow, And Stress Analysis In Phase-Change Problems. Numer. Heat Transf. Part B Fundam. 42, 437–459. https://doi.org/10.1080/10407790190054021.
Thomas, B.G., Moitra, A., McDavid, R., 1996. Simulation of longitudinal off - corner depressions in continuously - cast steel slabs. Iron Steelmak. (ISS Trans. 23, 143–156.
Thomas, B.G., Ojeda, C., 2003. Ideal taper prediction for slab casting. ISS Steelmaking Conference. ISS-AIME, Indianapolis, IN, pp. 295–308.
Venugopal, S., Mannan, S.L., Prasad, Y.V.R.K., 1993. Processing map for hot working of stainless steel type AISI 316L. Mater. Sci. Technol. 9, 899–906. https://doi.org/10.1179/mst.1993.9.10.899.
Wray, P.J., 1976. Plastic deformation of delta-ferritic iron at intermediate strain rates. Metall. Trans. A 7, 1621–1627. https://doi.org/10.1007/BF02817878.
Wray, P.J., 1982. Effect of Carbon Content on the Plastic Flow of Plain Carbon Steels at Elevated Temperatures. Metall. Mater. Trans. A 13, 125–134.
Weiner, J.H., Boley, B.A., 1963. Elasto-plastic thermal stresses in a solidifying body. J. Mech. Phys. Solids 1, 145–154. https://doi.org/10.1016/0022-5096(63)90049-8.
World Steel Association, 2017. Steel Statistical Yearbook 2017. pp. 128. http://www.worldsteel.org/statistics/statistics-archive/yearbook-archive.html.
Yuan, Q., Sivaramakrishnan, S., Vanka, S.P., Thomas, B.G., 2004. Computational and Experimental Study of Turbulent Flow in a 0. 4-Scale Water Model of a Continuous Steel Caster. Metall. Mater. Trans. B 35, 967–982.
Zappulla, M.L.S., 2016. Grade Effects on Thermal-Mechanical Behavior During the Initial Solidification of Continuously Cast Steels. Masters Thesis. The University of Illinois at Urbana-Champaign.
Zappulla, M.L.S., Hibbeler, L.C., Thomas, B.G., 2017. Effect of Grade on Thermal–Mechanical Behavior of Steel During Initial Solidification. Metall. Mater. Trans. A 48, 3777–3793. https://doi.org/10.1007/s11661-017-4112-z.
Zappulla, M.L.S., Thomas, B.G., 2017. Thermal-Mechanical Model of Depression Formation in Steel Continuous Casting. TMS 2017 146th Annual Meeting & Exhibition Supplemental Proceedings. pp. 501–510. https://doi.org/10.1007/978-3-319-51493-2_48. San Diego, CA.
Zhu, H., 1996. Coupled Thermo-Mechanical Finite-Element Model With Application to Initial Soldification. Ph.D. Thesis. The University of Illinois at Urbana-Champaignhttps://doi.org/10.1017/CBO9781107415324.004.